Efficient Parametric Uncertainty Analysis of an Earth Entry Vehicle Concept using Least Angle Regression

Thomas K. West IV* and Christopher O. Johnston†
NASA Langley Research Center, Hampton, VA, 23681

Nomenclature

$\mathcal{A}$	Active Set	S	Sobol Index
C	Absolute Maximum Correlation	$\boldsymbol{u}$	Equiangular Vector
c	Correlation	x	Deterministic Variables
D	Total Variance	α	Polynomial Chaos Expansion Coefficient
N_t	Number of Terms	γ	Update Magnitude
n	Number of Random Dimensions	ϵ	Surrogate Model Error
p	Polynomial Order	Ψ	Random Basis Function
R	Stochastic Response	ξ	Standard Input Random Variable
r	Least Angle Regression Predicted Response		

I. Introduction

As NASA begins the development of a Mars sample return mission, uncertainty quantification (UQ) will serve as a key capability for estimating risk and identifying key sources of uncertainty that drive margins. While an Earth entry vehicle (EEV) system as a whole is subject to significant uncertainty, the thermal protection system (TPS) is one of the subsystems that is plagued by numerous source of uncertainty due to the complex physics associated with both the aerothermodyamics modeling and the material response. A reliable TPS design is absolutely critical to ensuring not only the survival of the collected samples but also to avoid potentially contaminating the Earth due to the uncontrolled release of the samples by a compromised entry vehicle.

Previous work by Johnston et al. [1] investigated the impact of uncertainty on stagnation point convective and radiative heating predictions during hyperbolic Earth entry, similar to that of a Mars sample return mission. Their UQ approach was to assume the impact of uncertainty sources were independent from one another and that heating was monotonic with the uncertainty. This approach significantly reduced the number of simulations needed to obtain an overall heating uncertainty prediction but required assumptions with unknown impact. Additionally, Johnston and Kleb [2] performed a detailed uncertainty analysis of forebody radiative heating during lunar-return Earth entry using fuzzy set logic. This approach used a Cauchy deviates method, which required 10,000 evaluations of the computational model.

Following these previous works on UQ of planetary entry vehicle heating, West et al. [3] introduced a technique based on compressed sensing [4] and polynomial chaos. This optimization approach was shown to drastically reduce the computational cost of propagating numerous sources of uncertainty through an expensive computational model. West et al. [5] applied the compressed sensing based polynomial chaos approach to the analysis of radiative heating uncertainty on the Stardust sample return capsule backshell. While these past works both investigated the impact of uncertainty on heating predictions and reduced the computational cost of doing so, there is a strong need for less complex techniques and additional computational savings.

The overall objective of this work is to outline an approach to propagating numerous sources of uncertainty through a computationally expensive model. The approach is to use a technique termed least angle regression (LAR) [6] in conjunction with point-collocation based non-intrusive polynomial chaos (NIPC) [7]. This iterative approach to constructing a polynomial chaos representation of the uncertainty enables potentially significant computational saving

*Aerospace Engineer, Vehicle Analysis Branch, Systems Analysis and Concepts Directorate, Member AIAA.
†Aerospace Engineer, Aerothermodynamics Branch, Branch, Research Directorate, Associate Fellow AIAA.

over traditional sampling-based approaches, such as Monte Carlo. In addition to presenting this new approach, this paper provides comparisons between other uncertainty propagation approaches, such as compressed sensing, are made to highlight the LAR-NIPC approach.

The LAR-NIPC approach is applied to a computational fluid dynamics (CFD) model of convective and radiative heating on the surface of an EEV returning from Mars. Hundreds of parametric uncertainty sources are considered in this study. In the flow field, these include uncertainties in the chemical rate model for each reaction and uncertainties in the energy exchange cross section applied for neutral-electron collisions. Regarding prediction of convective heating, uncertainty in binary collision integrals used to approximate transport properties, the turbulent Schmidt number, and wall roughness height are considered. For radiation, atomic line strengths, Stark broadening widths, photoionization cross sections, molecular and oscillator strength uncertainties are considered. Additionally, for the EEV problem of interest, key uncertainty sources are identified that may serve as indicators for prioritizing future investments to reduce overall parametric uncertainty.

In the next section, the UQ approach used in this study is described in detail. Section III then outlines the CFD model used to simulate the EEV during entry into Earth's atmosphere. Section IV presents the results of this study including a description of the baseline forebody heating predictions, followed by details of the uncertainty analysis study. The last section highlights key findings from this work.

II. Uncertainty Quantification Approach

A. Generalized Polynomial Chaos

Polynomial chaos is a surrogate modeling technique based on a spectral representation of the uncertainty. An important aspect of spectral representations is the decomposition of a response value or random function R into a linear combination of separable deterministic and stochastic components, as shown in Eq. (1) for a polynomial of order p and dimension n.

$$R(\boldsymbol{x}, \boldsymbol{\xi}) \approx \sum_{i=0}^{N_t-1} \alpha_i(\boldsymbol{x}) \Psi_i(\boldsymbol{\xi}) + \epsilon \tag{1}$$

Here, α_i is the deterministic component, and Ψ_i is the random variable basis functions corresponding to the i^{th} mode. The basis functions, Ψ_i, of each random variable are determined using the Askey key [8] and are dependent on the distribution of each random variable. The response, R, is a function of independent, deterministic variables, $\boldsymbol{x}$, and n independent, standard random variables, $\boldsymbol{\xi}$. Note that this series is, by definition, an infinite series; however, in practice, it is truncated, and a sum is taken over a discrete number of output modes, leaving a finite truncation error, ϵ. To form a complete basis or a total order expansion, N_t terms are required, which can be computed from Eq. (2) for a polynomial chaos expansion (PCE) of order p and a number of random dimensions or variables, n.

$$N_t = \frac{(n+p)!}{n!p!} \tag{2}$$

Special consideration is needed when epistemic variables are present, which is the case in the present study. For epistemic variables with a bounded domain (i.e., intervals), the Legendre polynomials can serve as an appropriate basis, as they too have a bounded domain. Then, the second-order probability approach described by Eldred and Swiler [9] can be applied to propagate mixed uncertainty though the PCE and obtain intervals at select probability levels of interest. Further details on polynomial chaos theory is given by Ghanem and Spanos [10]. A description of more recent developments, including the analysis of mixed uncertainty with stochastic expansions is given by Eldred [11].

B. Point-Collocation, Non-Intrusive Polynomial Chaos

The objective with any PCE method is to determine the expansion coefficients, α_i. To do this, polynomial chaos methods can be implemented using an intrusive or a non-intrusive approach. While an intrusive method may appear straightforward in theory, for complex problems this process may be computationally expensive and difficult to implement as changing the deterministic model is required [12]. In contrast, the non-intrusive approach can be easily implemented to construct a surrogate model that represents a complex computational simulation because no modification to the deterministic model is required. The non-intrusive methods require only the response (or sensitivity [13–15]) values at selected sample points to approximate the stochastic response surface.

Several methods have been developed for NIPC. Of these, the point-collocation NIPC method has been used extensively in many aerospace simulation and CFD problems [7, 13, 16, 17] for improved computational efficiency and tractability for high-dimension problems over other spectral-projection-based approaches. The point-collocation method starts with replacing a stochastic response or random function with its PCE by using Eq. (1). N_s sample vectors are chosen in random space, and the deterministic code is evaluated at these points, which is the left hand side of Eq. (1). Following this, a linear system of N_s equations can be formulated and solved for the expansion coefficients of the PCE. This system is shown in Eq. (3).

$$\begin{pmatrix} R(\mathbf{x}, \boldsymbol{\xi}_1) \\ R(\mathbf{x}, \boldsymbol{\xi}_2) \\ \vdots \\ R(\mathbf{x}, \boldsymbol{\xi}_{N_s}) \end{pmatrix} = \begin{pmatrix} \Psi_0(\boldsymbol{\xi}_1) & \Psi_1(\boldsymbol{\xi}_1) & \cdots & \Psi_{N_t-1}(\boldsymbol{\xi}_2) \\ \Psi_0(\boldsymbol{\xi}_2) & \Psi_1(\boldsymbol{\xi}_2) & \cdots & \Psi_{N_t-1}(\boldsymbol{\xi}_2) \\ \vdots & \vdots & \ddots & \vdots \\ \Psi_0(\boldsymbol{\xi}_{N_s}) & \Psi_1(\boldsymbol{\xi}_{N_s}) & \cdots & \Psi_{N_t-1}(\boldsymbol{\xi}_{N_s}) \end{pmatrix} \begin{pmatrix} \alpha_0 \\ \alpha_1 \\ \vdots \\ \alpha_{N_t-1} \end{pmatrix} \tag{3}$$

Note that for this linear system, N_t is equal to the minimum number of deterministic samples, N_s, required to obtain a exact solution. If more linearly independent samples are available, the system is considered overdetermined and can be solved using a least squares approach. On the contrary, if the number samples is less than the number of terms in the PCE, N_t, then the linear system in Eq. (3) has infinitely many solutions. West et al. [3] proposed using compressed sensing [4] to seek out a solution with a minimum number of nonzero PCE coefficients. This approach, while highly effective and efficient, requires the solution of an L_1-minimization problem. A desired approach may be to obtain the same level of (or better) efficiency without relying on solving an optimization problem, which may induce error in the solution and subsequent uncertainty estimation.

C. Sparse Approximation via Least Angle Regression

One approach to obtaining a unique solution to an underdetermined linear system of equations is to use a technique called LAR. LAR was proposed by Efron et al. [6] as a means of efficiently obtaining the solution of a linear system with the minimum number of nonzero terms, similar to compressed sensing [3, 4]. However, the LAR approach does not require the solution of an optimization problem, which may reduce complexity and minimize potential error.

LAR is an iterative or stagewise procedure that incrementally adds terms to a polynomial model of the response. Here, that model is the polynomial chaos expansion. The number of terms added is based on the number of samples, N_s, available for the regression. LAR begins by setting a prediction vector, r to zero. The correlations, c_i, between the polynomial terms and the current residual between the training data, y, and the current LAR predicted responses is given by (4).

$$\boldsymbol{c} = \Psi' (\boldsymbol{y} - \boldsymbol{r}) \tag{4}$$

At each step in the iterative procedure, the set of active terms (or covariates), $\mathcal{A}$, contains the indices of PCE terms included in the current model (i.e., the columns of Ψ). At each iteration, the term with the absolute maximum correlation, defined by Eq. (5), to the training data is added to the active set.

$$C = \max_i \{|c_i|\} \tag{5}$$

After updating the active set with a new term, the next step is to update the prediction vector, r. To do this, LAR uses an equiangular step direction. The equiangular vector is defined by Eq. (6).

$$\boldsymbol{u}_{\mathcal{A}} = \Psi_{\mathcal{A}} \left(\mathbf{1}'_{\mathcal{A}} \left(\Psi'_{\mathcal{A}} \Psi_{\mathcal{A}} \right)^{-1} \mathbf{1}_{\mathcal{A}} \right)^{-1/2} \left(\Psi'_{\mathcal{A}} \Psi_{\mathcal{A}} \right)^{-1} \mathbf{1}_{\mathcal{A}} \tag{6}$$

Here, the vector of ones, $\mathbf{1}_{\mathcal{A}}$, has length equal to that of the active set (i.e., the number of terms in the current prediction). The prediction vector update is then given by Eq. (7).

$$\boldsymbol{r}_{\mathcal{A}_+} = \boldsymbol{r}_{\mathcal{A}} + \gamma \boldsymbol{u}_{\mathcal{A}} \tag{7}$$

The prediction update magnitude, γ, is defined by Eq. (8).

$$\gamma = \min_{i \in \mathcal{A}^c}{}^{+} \left\{ \frac{C - c_i}{A_{\mathcal{A}} - a_i}, \frac{C + c_i}{A_{\mathcal{A}} + a_{i\,i}} \right\} \tag{8}$$

Here, $A_{\mathcal{A}}$ and a_i are given by Eq. (9) and Eq. (10), respectively. Also, the + indicates only positive components for each i and $\mathcal{A}^c$ is the complement set to $\mathcal{A}$.

$$A_{\mathcal{A}} = \left(\mathbf{1}'_{\mathcal{A}} \left(\Psi'_{\mathcal{A}} \Psi_{\mathcal{A}} \right)^{-1} \mathbf{1}_{\mathcal{A}} \right)^{-1/2} \tag{9}$$

$$\boldsymbol{a} = \Psi' \boldsymbol{u}_{\mathcal{A}} \tag{10}$$

Starting with the active set $\mathcal{A}$ empty, the stagewise process outlined in Eqs. (6) through (10) is repeated, adding one term to the active set at each iteration. This is done until convergence of the predicted responses is observed, or all of the available training data are included in the active set. Note that the active set length is limited by the number of available training data. As the active set length approaches that of a full polynomial model, the LAR procedure tends to a least squares result and no additional error is incurred by including more data. The final LAR predicted response, $\boldsymbol{r}$, can then be used to estimate the PCE coefficients, $\boldsymbol{\alpha}$, by solving the linear system in Eq. (3) with only the terms in the active set.

For computationally expensive problems, monitoring convergence of the PCE model as the LAR approach progresses is the key to reducing computationally cost. Stopping the procedure when an acceptable level of error is achieved may limit the number of times a computational model needs to be executed. With the LAR approach, even one training point will return a result. However, enough data should be included to reach a desired level of convergence in the polynomial chaos model. Note that adaptive sampling approaches are the subject of future work. In this study, a large sample set of points are chosen from a Latin Hypercube design and points are randomly added to the set of training data.

D. Least Angle Regression Convergence

While monitoring the coefficients individually would be ideal, this may be unrealistic for large problems with hundreds or thousands of terms. Test points and cross validation approaches may be feasible but are often subject to significant error, particularly for small sample sizes. In this work, the approach was to track convergence of the total Sobol index [18] values for each uncertain variable. Because these values are based on the polynomial model terms directly, they are ideal for monitoring convergence. Sobol indices can be derived via *Sobol Decomposition*, which is a variance-based global sensitivity analysis method. First, the total variance, D, can be written in terms of the PCE, as shown in Eq. (11).

$$D = \sum_{j=1}^{P} \alpha_j^2(t, \vec{x}) \left\langle \Psi_j^2(\vec{\xi}) \right\rangle \tag{11}$$

Then, as shown by Sudret [18], the total variance can be decomposed as:

$$D = \sum_{i=1}^{i=n} D_i + \sum_{1 \le i < j \le n}^{i=n-1} D_{i,j} + \sum_{1 \le i < j < k \le n}^{i=n-2} D_{i,j,k} + \cdots + D_{1,2,\ldots,n} \tag{12}$$

where the partial variances ($D_{i_1,\ldots,i_s}$) are given by:

$$D_{i_1,\ldots,i_s} = \sum_{\beta \in \{i_1,\ldots,i_s\}} \alpha_\beta^2 \left\langle \Psi_\beta^2(\vec{\xi}) \right\rangle, \qquad 1 \le i_1 < \ldots < i_s \le n \tag{13}$$

Then the Sobol indices ($S_{i_1 \cdots i_s}$) are defined as,

$$S_{i_1 \cdots i_s} = \frac{D_{i_1,\ldots,i_s}}{D} \tag{14}$$

which satisfy the following equation:

$$\sum_{i=1}^{i=n} S_i + \sum_{1 \le i < j \le n}^{i=n-1} S_{i,j} + \sum_{1 \le i < j < k \le n}^{i=n-2} S_{i,j,k} + \cdots + S_{1,2,\ldots,n} = 1.0 \tag{15}$$

The Sobol indices provide a sensitivity measure due to individual contribution from each input uncertain variable, S_i, as well as the mixed contributions ($\{S_{i,j}\}, \{S_{i,j,k}\}, \cdots$). As shown by Sudret [18], the total (combined) effect,S_{T_i}, of an input parameter i is defined as the summation of the partial Sobol indices that include the particular parameter:

$$S_{T_i} = \sum_{L_i} \frac{D_{i_1,\ldots,i_s}}{D}; \quad L_i = \{(i_1,\ldots,i_s) : \exists\ k,\ 1 \le k \le s,\ i_k = i\} \tag{16}$$

For example, with $n = 3$, the total contribution to the overall variance from the first uncertain variable ($i = 1$) can be written as:

$$S_{T_1} = S_1 + S_{1,2} + S_{1,3} + S_{1,2,3} \tag{17}$$

From these formulations, it can be seen that the Sobol indices can be used to provide a relative ranking of each input uncertainty to the overall variation in the output with the consideration of nonlinear correlation between input variables and output quantities of interest.

The accuracy of the Sobol indices depends highly on the PCE coefficients, making them an ideal measure of PCE convergence. Also, because the number of total Sobol indices is the same as the number of uncertain parameters, n, there are less parameters to track, as $n < N_t$ for a total order expansion. Tracking Sobol indices also enables a global ranking of each uncertain variable in terms of relative contribution to the total predicted uncertainty. This may be particularly useful for dimension reduction strategies [3, 13] and to help guide investments into effectively reducing uncertainty with future efforts.

III. Computational Modeling Approach and Sources of Uncertainty

This section describes the CFD model used to predict the convective and radiative heating on the surface of an EEV concept. The first section details the geometry and the computational domain used in this study. The next section describes the CFD model, followed by a detailed description of the uncertainty sources considered in this study.

A. Geometry and Computational Domain

The aeroshell geometry was a 45 deg. sphere-cone with a 0.3 meter nose radius and a base diameter of 1.3 meters. Images of the geometry used in this study are given in Fig.1. The computational domain was axisymmetric about the centerline with 153 nodes in the streamwise direction and 121 nodes normal to the wall. The grid for the final solution is shock-aligned with 80% of the grid normal to the wall lying inside the shock layer. The wall normal spacing was achieved via grid adaption to achieve a cell Reynolds number of 1.0. Measures of grid convergence for both radiative and convective heating will be included in the final manuscript.

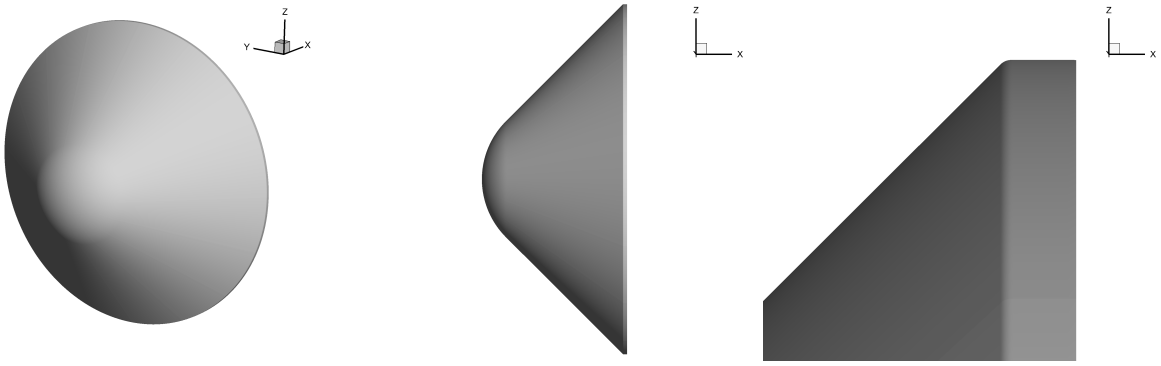

(a) Isometric view. (b) Side view. (c) Shoulder.

Fig. 1 Earth entry vehicle conceptual geometry.

B. Computational Fluid Dynamics Model

In the current study, the flowfield was modeled using the Langley Aerothermodynamic Upwind Relaxation Algorithm (LAURA) software, which is a finite-volume, Navier-Stokes flow solver [19]. LAURA uses a second-order, upwind, discretization scheme with Roe's flux-difference splitting and Yee's Symmetric Total Variation Diminishing (STVD)

Table 1 Flowfield dissociation reactions.

#	Reaction	$A_{f,i}\left(\frac{cm^3}{mol-s}\right)$	$n_{f,i}$	$D_{f,i}(K)$	$T_{f,i}$	Third Body, M	Uncertainty
	Dissociation Reactions						
1	$N_2 + M \leftrightarrow 2N + M$	3.01e+22	−1.60	1.132e+05	T_a	H, C, O, N	+1, -1 om
		7.000e+21	−1.60	1.132e+05	T_a	others	+1, -1 om
2	$NO + M \leftrightarrow N + O + M$	4.567e+17	0.00	7.550e+04	T_a	H, C, N, O, NO, CO2	+1, -1 om
		2.080e+16	0.00	7.550e+04	T_a	others	+1, -1 om
3	$O_2 + M \leftrightarrow 2O + M$	1.000e+22	−1.50	5.936e+04	T_a	H, C, O, N	+50, -50%
		2.000e+21	−1.50	5.936e+04	T_a	others	+50, -50%
	Exchange Reactions						
4	$N_2 + O \leftrightarrow NO + N$	6.0e+13	0.1	3.800e+04	T_{tr}		+50, -50%
5	$O_2 + N \leftrightarrow NO + O$	2.49e+9	1.18	4.005e+03	T_{tr}		+1, -1 om
	Ionization Reactions						
6	$N + N \leftrightarrow N_2^+ + e^-$	4.400e+07	1.50	6.750e+04	T_{ve}		+1, -1 om
7	$N + O \leftrightarrow NO^+ + e^-$	5.300e+12	0.00	3.190e+04	T_{ve}		+1, -1 om
8	$N + e^- \leftrightarrow N^+ + e^- + e^-$	2.50e+34	−3.82	1.682e+05	T_{ve}		+1, -1 om
9	$N^+ + N_2 \leftrightarrow N_2^+ + N$	1.000e+12	0.50	1.220e+04	T_{ve}		+1, -1 om
10	$N_2 + O^+ \leftrightarrow N_2^+ + O$	9.100e+11	0.36	2.280e+04	T_{tr}		+1, -1 om
11	$N_2 + e^- \leftrightarrow 2N + e^-$	6.0e+3	2.6	1.132e+5	T_{ve}		+1, -1 om
12	$NO + O^+ \leftrightarrow N^+ + O_2$	1.400e+05	1.90	2.660e+04	T_{tr}		+1, -1 om
13	$NO^+ + N \leftrightarrow N_2^+ + O$	7.200e+13	0.00	3.550e+04	T_{tr}		+1, -1 om
14	$NO^+ + N \leftrightarrow O^+ + N_2$	3.400e+13	−1.08	1.280e+04	T_{tr}		+1, -1 om
15	$NO^+ + O \leftrightarrow N^+ + O_2$	1.000e+12	0.50	7.720e+04	T_{tr}		+1, -1 om
16	$NO^+ + O \leftrightarrow O_2^+ + N$	7.200e+12	0.29	4.860e+04	T_{tr}		+1, -1 om
17	$NO^+ + O_2 \leftrightarrow NO + O_2^+$	2.400e+13	0.41	3.260e+04	T_{tr}		+1, -1 om
18	$O + O \leftrightarrow O_2^+ + e^-$	7.100e+02	2.70	8.060e+04	T_{ve}		+1, -1 om
19	$O + e^- \leftrightarrow O^+ + e^- + e^-$	3.900e+33	−3.78	1.585e+05	T_{ve}		+1, -1 om
20	$O_2^+ + N \leftrightarrow O_2 + N^+$	8.700e+13	0.14	2.860e+04	T_{tr}		+1, -1 om
21	$O_2^+ + N_2 \leftrightarrow N_2^+ + O_2$	9.900e+12	0.00	4.070e+04	T_{tr}		+1, -1 om
22	$O_2^+ + O \leftrightarrow O^+ + O_2$	4.000e+12	−0.09	1.800e+04	T_{tr}		+1, -1 om

formulation of the inviscid flux. The flowfield was assumed to be steady state, and the boundary layer was modeled as fully-turbulent employing the Baldwin-Lomax algebraic turbulence model [20]. Additionally, a roughness augmentation model described by Krogstad [21] was used to model a mean wall roughness height of 0.7 millimeters.

The gas properties were modeled with a thermochemical nonequilibrium assumption using the two temperature model [22, 23]. Freestream mass fractions were assumed to be 76% N_2 and 24% O_2. Modeled flowfield species included N_2, O_2, N_2^+, O_2^+, N, O, N^+, O^+, NO, NO^+, and e^-. The chemical rate model used in this study is given in Table 1. Note that the parameters in this table are those of an Arrhenius form. The forward reaction rate for each mechanism was computed with Eq. (18). The wall temperature was calculated by assuming radiative equilibrium with a non-ablating and fully-catalytic to homogeneous recombination wall boundary condition.

$$k_{f,i} = A_{f,i} T_{f,i}^{n_{f,i}} exp(-D_{f,i}/T_{f,i}) \tag{18}$$

The radiation was modeled using the High-Temperature Aerothermodynamic Radiation (HARA) code [24, 25]. HARA uses atomic levels and lines obtained from the National Institute of Standards and Technology (NIST) database [26], Opacity Project databases [27], and atomic bound-free (photoionization) cross-sections from the TOPbase [28]. The molecular radiation mechanisms modeled in the current study are presented in Table 2. Molecular band systems are modeled using the smeared-rotational band approach (SRB). This approximation is shown by Johnston et al. [1, 24] to result in errors of less than 3% for air shock layers.

Additionally, spectral line and continuum radiation from excited N and O are also modeled. HARA uses a Collisional Radiative (CR) or non-Boltzmann modeling of atomic and molecular electronic states. The non-Boltzmann approach used in this study is described by Johnston et al. [29]. Coupled radiation was modeled in the flowfield energy equations. A ray-tracing approach [30] was applied for computing the radiative heating at the wall, while the tangent-slab approach was used to compute the divergence of the radiative flux, unless noted otherwise.

Table 2 Molecular radiation mechanisms.

Molecule	Band Name	Uncertainty
N_2	First-Positive	+/- 10%
N_2	Second-Positive	+/- 10%
N_2	Birge-Hopfield I	+/- 10%
N_2	Birge-Hopfield II	+/- 10%
N_2	Worley Jenkins	+/- 10%
N_2^+	First-Negative	+/- 10%
NO	Beta	+/- 50%
NO	Delta	+/- 50%
NO	Epsilon	+/- 50%
NO	Gamma	+/- 50%
NO	Beta Prime	+/- 50%
NO	Gamma Prime	+/- 50%

C. Sources of Uncertainty

Numerous, parametric uncertainty sources were considered in this study. In the flow field, these include uncertainties in the chemical rate model for each reaction and uncertainties in the energy exchange cross section applied for neutral-electron collisions. Regarding prediction of convective heating, uncertainty in binary collision integrals used to approximate transport properties, the turbulent Schmidt number, and wall roughness height were considered. For radiation, atomic line strengths, Stark broadening widths, photoionization cross sections, molecular and oscillator strength uncertainties were considered. Details of each uncertainty sources and associated reference will be included in the final manuscript.

IV. Results and Discussion

In this section, the results of the present, study are presented, along with discussion of key findings. First, the baseline or nominal solution of the EEV forebody flow field is described. Then, the uncertainty in predicted convective and radiative heating is given, based on the LAR approach outlined in section II. Key sources of uncertainty are identified, and a comparison with alternative uncertainty propagation approaches is provided.

A. Baseline Solution

The conditions of interest in this study are those taken from a probable reference trajectory of a Mars sample return vehicle. Peak heating during a non-lifting (zero angle of attack) ballistic entry occurred when the freestream velocity, density, and temperature were approximately 10.256 km/s, 1.43e-3 kg/m^3, 263.9 K, respectively, and were the flight conditions of interest here. At these Earth entry conditions, near complete dissociation of freestream N_2 in the post-shock flow around the nose of the vehicle was predicted with partial dissociation occurring along the flank region along the body. Additionally, ionization of N occurs near the stagnation region of the flow. This is illustrated in Fig.2.

Similarly, near complete O_2 dissociation is predicted in the entire post-shock flow along the body. Ionization of O also occurs in the stagnation region of the flow. This is illustrated in Fig.3. There is additional formation of NO and trace NO^+ in the thermodynamic nonequilibrium region near the shock. This occurs primarily along the vehicle flank, where the peak NO mass fraction is about 0.04. Away from the shock, the NO mass fraction falls at least an order of magnitude within the shock layer.

Convective and radiation heating rates, as well as wall temperature are shown in Fig.4. The inclusion of both turbulent and roughness augmentation along the surface significantly increases the convective heating along the flank region compared to smooth wall, laminar boundary layer model. The latter would result in peak convective heating being at the stagnation point. As a result of the convective heating, the wall reaches a radiative equilibrium temperature of about 5000 K near the shoulder. Note that this temperature is remarkably high. Modeling ablation of the surface would certainly lower this temperature. Including an ablation model for an appropriate thermal protection material system is the subject of future work.

The radiative heating, shown in more detail in Fig.5, primarily occurs on the vehicle nose, with the peak being at the stagnation point. In total, radiative heating makes up about 20% of the total stagnation point heating. Also, Fig.5 shows a comparison of the primarily used ray-tracing model for computing wall radiative heating with the traditional tangent-slab approach. Overall, the tangent-slab approach results in an over-prediction of radiative heating by 10-12%

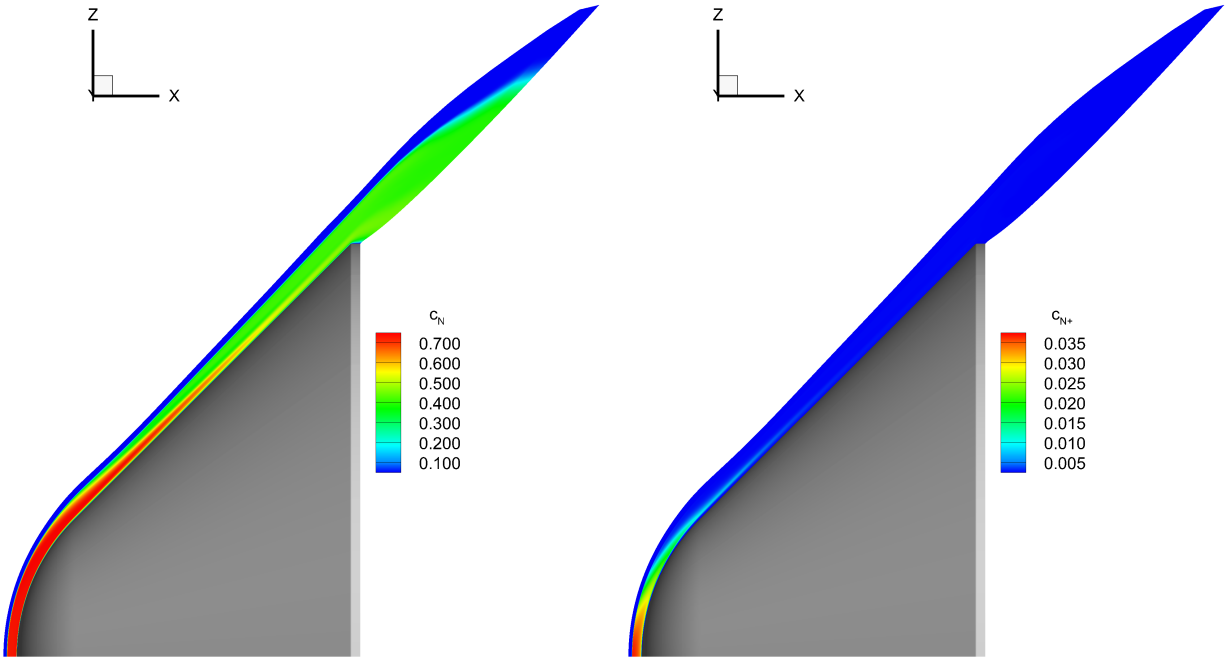

(a) Atmoic Nitrogen.

(b) Ionized Nitrogen.

Fig. 2 Contours of atomic and ionized N mass fractions.

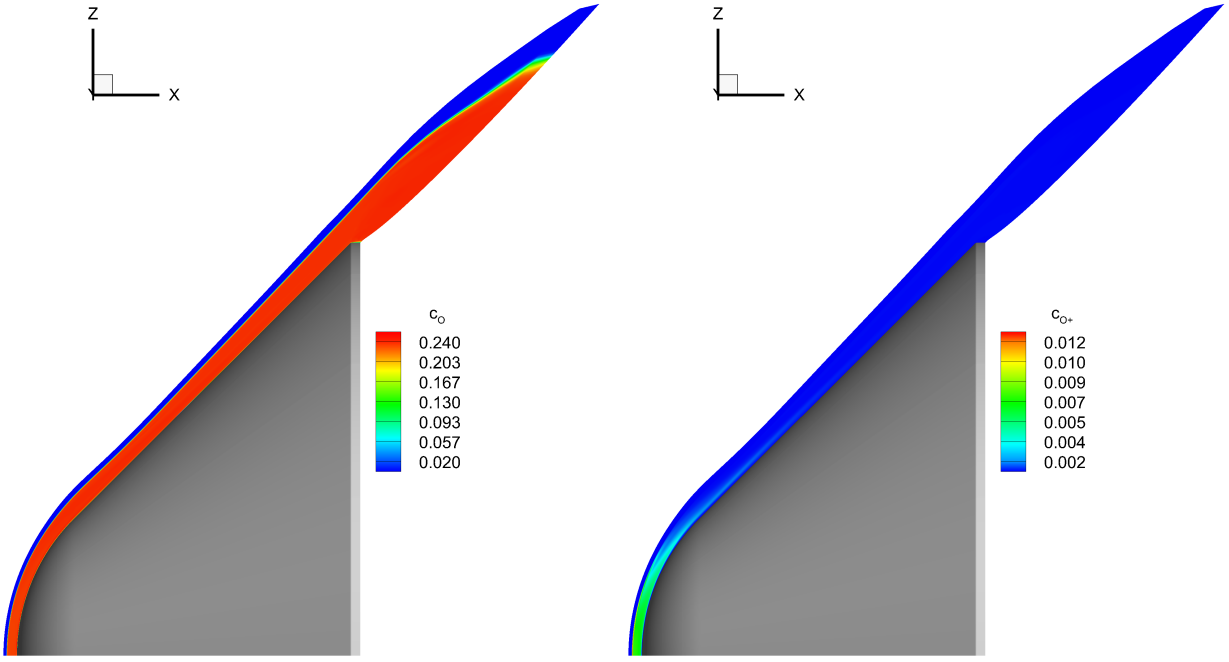

(a) Atmoic Oxygen.

(b) Ionized Oxygen.

Fig. 3 Contours of atomic and ionized O mass fractions.

along most of the body. The exceptions being around 0.075 meters, which is the sphere-cone juncture, and at the shoulder. At the sphere-cone juncture, the impact of the stagnation region radiation contributes to overall radiative

heating away from the stagnation point, which is not captured by the tangent-slab model. Moving towards the shoulder, along the flank, the flow is much less tangent-slab like. Therefore, the rise in error is not unexpected.

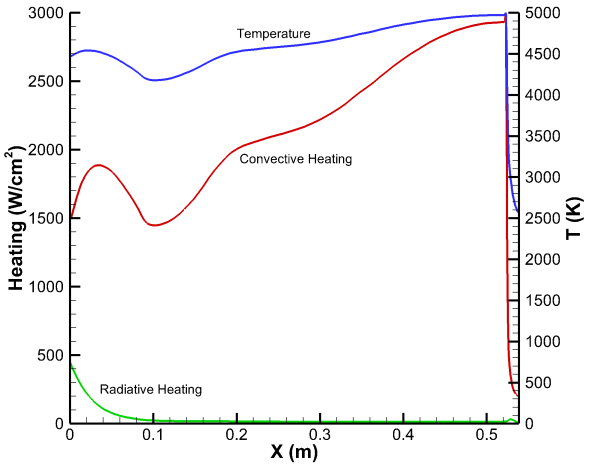

Fig. 4 Surface heating and temperature distributions.

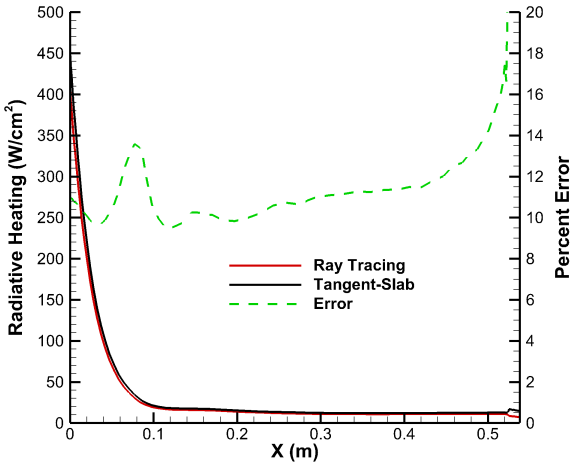

Fig. 5 Comparison of ray-tracing and tangent-slab based radiative heating rates.

Specific details of the radiative heating, including contributions of individual species, can be extracted from the radiative flux spectrum, which is shown in Fig.6 for the stagnation point. Radiation reaching the wall primarily comes from two sources: N line emission and N photoionization. Photoionization occurs mostly in the 0-2 eV range. Atomic line emission occurs in both the 0-3 eV and the 9-11 eV ranges. Note that the inclusion of ablation would introduce species that provide additional absorption of atomic line emission, particularly in the 5-12 ev range when considering a carbon-phenolic like ablator. More details of the relative impact of photoionization to atomic line emission and impact of coupled ablation are discussed by Johnston et al. [1]

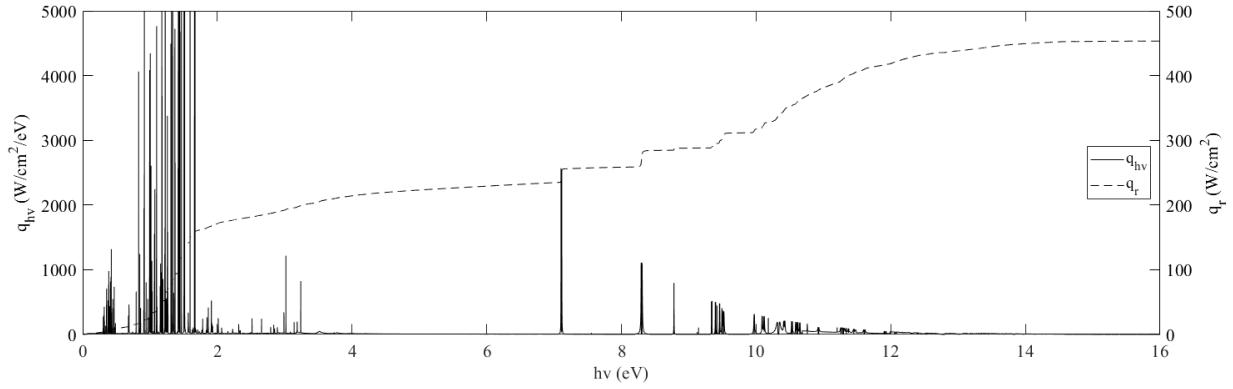

Fig. 6 Stagnation point radiative flux spectrum.

V. Additions to the Final Manuscript

Additions to the final manuscript will include a detailed uncertainty analysis using the outlined least angle regression approach. Implicitly, key sources of uncertainty will be identified for future investment opportunities. Comparisons to other uncertainty quantification approaches will also be made.

Acknowledgments

References

[1] Johnston, C. O., Mazaheri, A., Gnoffo, P., Kleb, B., and Bose, D., "Radiative Heating Uncertainty for Hyperbolic Earth Entry, Part 1: Flight Simulation Modeling and Uncertainty," *Journal of Spacecraft and Rockets*, Vol. 50, No. 1, 2013, pp. 19–38. doi:10.2514/1.A32254.

[2] Johnston, C. O., and Kleb, B., "Uncertainty Analysis of Air Radiation for Lunar-Return Shock Layers," *Journal of Spacecraft and Rockets*, Vol. 49, No. 3, 2012, pp. 425–434.

[3] West, T. K., and Hosder, S., "Uncertainty Quantification of Hypersonic Reentry Flows with Sparse Sampling and Stochastic Expansions," *Journal of Spacecraft and Rockets*, Vol. 52, No. 1, 2015, pp. 120–133. doi:10.2514/1.A32947.

[4] Donoho, D. L., "Compressed Sensing," *IEEE Transactions on Information Theory*, Vol. 52, No. 4, 2006, pp. 1289–1306. doi:10.1109/TIT.2006.871582.

[5] West, T. K., Johnston, C. O., and Hosder, S., "Uncertainty and Sensitivity Analysis of Afterbody Radiative Heating Predictions for Earth Entry," *Journal of Thermophysics and Heat Transfer*, Vol. 31, No. 2, 2017, pp. 294–306. doi:10.2514/1.T4948.

[6] Efron, B., Hastie, T., Johnstone, I., and Tibshirani, R., "Least angle regression," *The Annals of Statistics*, Vol. 32, No. 2, 2004, pp. 407 – 499. doi:10.1214/009053604000000067.

[7] Hosder, S., Walters, R. W., and Balch, M., "Point-Collocation Nonintrusive Polynomial Chaos Method for Stochastic Computational Fluid Dynamics," *AIAA Journal*, Vol. 48, No. 12, 2010, pp. 2721–2730. doi:10.2514/1.39389.

[8] Xiu, D., and Karniadakis, G., "The Wiener–Askey Polynomial Chaos for Stochastic Differential Equations," *SIAM Journal on Scientific Computing*, Vol. 24, No. 2, 2002, pp. 619–644. doi:10.1137/S1064827501387826.

[9] Swiler, L. P., and Eldred, M. S., "Efficient algorithms for mixed aleatory-epistemic uncertainty quantification with application to radiation-hardened electronics. Part I, algorithms and benchmark results." , September 2009. doi:10.2172/972887.

[10] Ghanem, R. G., and Spanos, P. D., *Stochastic Finite Elements: A Spectral Approach*, Springer-Verlag, New York, 1991. doi:10.1007/978-1-4612-3094-6.

[11] Eldred, M. S., "Recent Advances in Non-Intrusive Polynomial Chaos and Stochastic Collocation Methods for Uncertainty Analysis and Design," AIAA Paper 2009-2274, 2009. doi:10.2514/6.2009-2274.

[12] Hosder, S., and Bettis, B., "Uncertainty and Sensitivity Analysis for Reentry Flows with Inherent and Model-Form Uncertainties," *Journal of Spacecraft and Rockets*, Vol. 49, No. 2, 2012, pp. 193–206. doi:10.2514/1.A32102.

[13] West, T. K., Hosder, S., and Johnston, C. O., "Multistep Uncertainty Quantification Approach Applied to Hypersonic Reentry Flows," *Journal of Spacecraft and Rockets*, Vol. 51, No. 1, 2014, pp. 296–310. doi:10.2514/1.A32592.

[14] Lockwood, B., and Mavriplis, D., "Gradient-based methods for uncertainty quantification in hypersonic flows," *Computers and Fluids*, Vol. 85, 2013, pp. 27 – 38. doi:10.1016/j.compfluid.2012.09.003.

[15] Roderick, O., Anitescu, M., and Fischer, P., "Polynomial Regression Approaches Using Derivative Information for Uncertainty Quantification," *Nuclear Science and Engineering*, Vol. 164, No. 2, 2010, pp. 122–139. doi:10.13182/NSE08-79.

[16] Bettis, B., Hosder, S., and Winter, T., "Efficient Uncertainty Quantification in Multidisciplinary Analysis of a Reusable Launch Vehicle," AIAA Paper 2011-2393, 2011. doi:10.2514/6.2011-2393.

[17] Han, D., and Hosder, S., "Inherent and Model-Form Uncertainty Analysis for CFD Simulation of Synthetic Jet Actuators," AIAA Paper 2012-0082, 2012. doi:10.2514/6.2012-82.

[18] Sudret, B., "Global sensitivity analysis using polynomial chaos expansions," *Reliability Engineering & System Safety*, Vol. 93, No. 7, 2008, pp. 964 – 979. doi:10.1016/j.ress.2007.04.002.

[19] Thompson, K. B., Hollis, B. R., Johnston, C. O., Kleb, B., Lessard, V. R., and Mazaheri, A., "LAURA Users Manual: 5.6," Tech. rep., NASA/TM-2020-2220566, Feb. 2020.

[20] Baldwin, B., and Lomax, H., "Thin-layer approximation and algebraic model for separated turbulentflows," AIAA Paper 1978-257, 1978. doi:10.2514/6.1978-257.

[21] Krogstad, P.-A., "Modification of the van Driest damping function to include the effects of surface roughness," *AIAA Journal*, Vol. 29, No. 6, 1991, pp. 888–894. doi:10.2514/3.10675.

[22] Gnoffo, P. A., Gupta, R. N., and Shinn, J. L., "Conservation Equations and Physical Models for Hypersonic Air Flows in Thermal and Chemical Nonequilibrium," Tech. rep., NASA TP 2867, Feb. 1989.

[23] Park, C., Howe, J. T., Jaffe, R. L., and Candle, G. V., "Review of Chemical-Kinetic Problems for Future NASA Missions, II: Mars Entries," *Journal of Thermophysics and Heat Transfer*, Vol. 8, No. 1, 1994, pp. 9–23.

[24] Johnson, C. O., Hollis, B. R., and Sutton, K., "Spectrum Modeling for Air Shock-layer Radiation at Lunar-Return Conditions," *Journal of Spacecraft and Rockets*, Vol. 45, No. 5, 2008, pp. 865–878.

[25] Johnson, C. O., Hollis, B. R., and Sutton, K., "Non-Boltzman Modeling for Air Shock Layers at Lunar Return Conditions," *Journal of Spacecraft and Rockets*, Vol. 45, No. 5, 2008, pp. 879–890.

[26] Ralchenko, Y., "NIST Atomic Spectra Database, Version 3.1.0," ???? URL `physics.nist.gov/PhysRefData/ASD/`.

[27] The Opacity Project Team, *The Opacity Project*, Vol. 1, 1995.

[28] Cunto, W., Mendoza, C., Ochsenbein, F., and Zeippen, C., "TOPbase at the CDS," *Astronomy and Astrophysics*, Vol. 275, 1993, pp. L5–L8.

[29] Johnston, C. O., Brandis, A. M., , and Sutton, K., "Shock Layer Radiation Modeling and Uncertainty for Mars Entry, AIAA 2012-2866," 43^{rd} *AIAA Thermophysics Conference*, New Orleans, LA, 2012.

[30] Mazaheri, A., Johnston, C. O., and Sefidbakht, S., "Three-Dimensional Radiation Ray-Tracing for Shock-Layer Radiative Heating Simulations," *Journal of Spacecraft and Rockets*, Vol. 50, No. 3, 2013, pp. 485–493.